Corrosion of 310 Stainless Steel in H_2-H_2O-H_2S Gas Mixtures: Studies at Constant Temperature and Fixed Oxygen Potential

D. BHOGESWARA RAO, K. T. JACOB, and HOWARD G. NELSON

Corrosion of SAE 310 stainless steel in H_2-H_2O-H_2S gas mixtures was studied at a constant temperature of 1150 K. Reactive gas mixtures were chosen to yield a constant oxygen potential of approximately 6×10^{-13} Nm^{-2} and sulfur potentials ranging from 0.19×10^{-2} Nm^{-2} to 33×10^{-2} Nm^{-2}. The kinetics of corrosion were determined using a thermobalance, and the scales were analyzed using metallography, scanning electron microscopy, and energy dispersive X-ray analysis. Two corrosion regimes, which were dependent on sulfur potential, were identified. At high sulfur potentials ($P_{S_2} \geq 2.7 \times 10^{-2}$ Nm^{-2}) the corrosion rates were high, the kinetics obeyed a linear rate equation, and the scales consisted mainly of sulfide phases similar to those observed from pure sulfidation. At low sulfur potentials ($P_{S_2} \leq 0.19 \times 10^{-2}$ Nm^{-2}) the corrosion rates were low, the kinetics obeyed a parabolic rate equation, and scales consisted mainly of oxide phases. Thermochemical diagrams for the Fe-Cr-S-O, Fe-Ni-S-O, Cr-Ni-S-O, and Si-Cr-S-O systems were constructed, and the experimental results are discussed in relation to these diagrams. Based on this comparison, reasonable corrosion mechanisms were developed. At high sulfur potentials, oxide and sulfide phases initially nucleate as separate islands. Overgrowth of the oxide by the sulfide occurs and an exchange reaction governs the corrosion process. Preoxidation at low oxygen potentials and 1150 K is beneficial in suppressing sulfidation at high sulfur potentials.

I. INTRODUCTION

THE internal components of coal gasifiers are exposed to hostile environments and elevated temperatures. The complex gaseous environments comprise molecular species that include oxygen, hydrogen, carbon, nitrogen, and sulfur. Various chemical species of the gas phase react collectively with the construction materials and degrade the structural integrity of the coal conversion systems. Of all the gaseous species present, hydrogen sulfide is probably the most corrosive component. A systematic study on the sulfidation of 310 stainless steel,[1,2,3] one of the candidate materials widely used in the pilot plant operations, indicated that the high reaction rates are a result of the sulfide scales being multilayered and nonprotective. Commercial steels are developed primarily for operation at high oxygen potentials. Therefore, characterization of their corrosion behavior in multicomponent gaseous environments at elevated temperatures is lacking. Such systematic studies are necessary for optimum selection of corrosion resistant alloys for coal gasification operations. As a part of a continuing study of corrosion problems associated with the internal components of coal gasifiers, the mechanism of corrosion of 310 stainless steel in gas mixtures of hydrogen, water vapor, and hydrogen sulfide is being investigated. This paper deals with the specific influence of sulfur potential (partial pressure) at a constant temperature of 1150 K and a fixed oxygen potential of approximately 6×10^{-13} Nm^{-2} on the kinetics of scale formation and on the composition and morphology of scale layers. Thermochemical diagrams have been constructed, and the experimental results are compared with those predicted. Based on the experimental results and the thermochemical diagrams, a tentative mechanism for the corrosion of 310 stainless steel has been proposed.

D. BHOGESWARA RAO, formerly a Senior Scientist with Materials and Molecular Research Division, Lawrence Berkeley Laboratory, Berkeley, CA 94720, is now Project Leader, Research and Development Section, Hewlett-Packard Company, Cupertino Integrated Circuits Operation, 10900 Wolfe Road, Cupertino, CA 95014. K. T. JACOB is Associate Professor, Department of Metallurgy and Materials Science, University of Toronto, Toronto, Canada M5S 1A4. HOWARD G. NELSON is Chief, Materials Science and Applications Office, NASA-Ames Research Center, Moffett Field, CA 94035.

Manuscript submitted April 8, 1981.

II. EXPERIMENTAL

A. *Materials*

Test coupons $2.5 \times 1.25 \times 0.33$ cm were prepared from a commercially produced cold-rolled, SAE 310 stainless steel. The composition of this alloy and the sample preparation procedures were given in an earlier publication.[1] The test coupons were polished through 5-μm-diamond abrasive and degreased thoroughly by washing in acetone. The surface area of each coupon was calculated to an accuracy of 1×10^{-5} cm^2 by using dimensions obtained with a micrometer.

Commercially available high-purity (Matheson) hydrogen, hydrogen sulfide, and argon were used; they were further purified by passing them through purification trains designed to remove residual water vapor and oxygen. Water vapor was introduced into the gas stream by bubbling argon through a saturator kept at a constant temperature. Gas flow rates were monitored and controlled by electronic linear mass flow controllers (Matheson). The oxygen and sulfur potentials were calculated from the ratios of hydrogen to water vapor and of hydrogen to hydrogen sulfide, using the equilibrium relationships, respectively,

$$H_2O(g) = H_2(g) + \frac{1}{2} O_2(g) \quad [1]$$

$$H_2S(g) = H_2(g) + \frac{1}{2} S_2(g) \quad [2]$$

The free energy functions for these calculations were taken from the JANAF Thermochemical Tables.[4] Oxygen potential of each run was also measured continuously by passing the gas mixture (H_2-H_2O-Ar) through an oxygen probe (Applied Electrochemistry Inc.). Hydrogen sulfide was introduced into the gas stream after the rest of the gases passed through the oxygen probe. The agreement between the measured and calculated oxygen potential was fair, and differed by not more than 10 pct (in most cases the agreement is within 5 pct). Hydrogen sulfide was removed from the exit gases by scrubbing through a sodium hydroxide solution before they were released to the atmosphere.

B. *Apparatus and Procedure*

The apparatus and the experimental procedure adopted in this study are essentially the same as those described previously,[2] except for a few minor changes made to avoid premature condensation of water vapor before it reached the reaction chamber. A schematic diagram of the apparatus is shown in Figure 1.

The kinetics of corrosion were measured using thermogravimetric analysis. Weight changes were continuously monitored to a sensitivity of 0.1 mg, using an AINSWORTH analytical balance unit. The balance system was purged with argon to avoid contamination of balance parts with sulfur and water vapor. A recrystallized alumina tube, 5 cm in diameter, served as a reaction chamber. The chamber was connected to the balance unit by means of a Teflon ring seal. All parts other than the reaction chamber were made of stainless steel. Gold-plated copper seals were used. A resistance furnace was used to heat the reaction chamber. Temperature was controlled by a potentiometric controller in conjunction with a Chromel-Alumel thermocouple positioned close to the furnace windings. Temperature was uniform within $\pm 1°$ over the middle 5 cm of the reaction tube. The actual coupon temperature was measured by means of a Pt-Pt/10 pct Rh thermocouple located near the coupon. It is estimated that coupon temperature was kept constant to better than $\pm 3°$ during all runs.

The test coupon, suspended from one arm of the balance by an alumina-sheathed platinum wire, was lowered into the constant-temperature zone of the reaction chamber. The coupon was brought to the desired temperature under a vacuum of less than 10^{-5} Nm^{-2}. Argon was then passed through the balance assembly, and at the same time hydrogen was passed through the reaction chamber to reduce any oxide traces that might have formed during handling of the coupon. The reaction gases, at the desired ratios of hydrogen to hydrogen sulfide to water vapor, were allowed to mix in a mixing chamber. The introduction of the reactive gas mixture into the reaction chamber was considered to be the start of the reaction. During all experiments a constant reactive gas flow rate of 1000 cm^3 min^{-1} or greater was maintained. At the end of each run the flow of reactive gas was halted, and argon flow was resumed while the coupon was being cooled. When the system had attained room temperature, the coupon was removed and the corrosion product was examined. Additionally, some test samples were quenched from the reaction temperature in order to facilitate identification of reaction products formed at high temperatures, thus avoiding disproportionation of reaction products during slow cooling. The continuously recorded weight-gain data were converted to weight-gain per unit area and used to calculate appropriate reaction rates. Each experiment was repeated at least four times and the repeatability of the results was better than ± 10 pct. At the end of the experiment, the coupon was sectioned with a diamond saw, mounted, polished, and examined metallographically and by scanning electron microscopy. The compositions of the scales were determined by energy dispersive X-ray

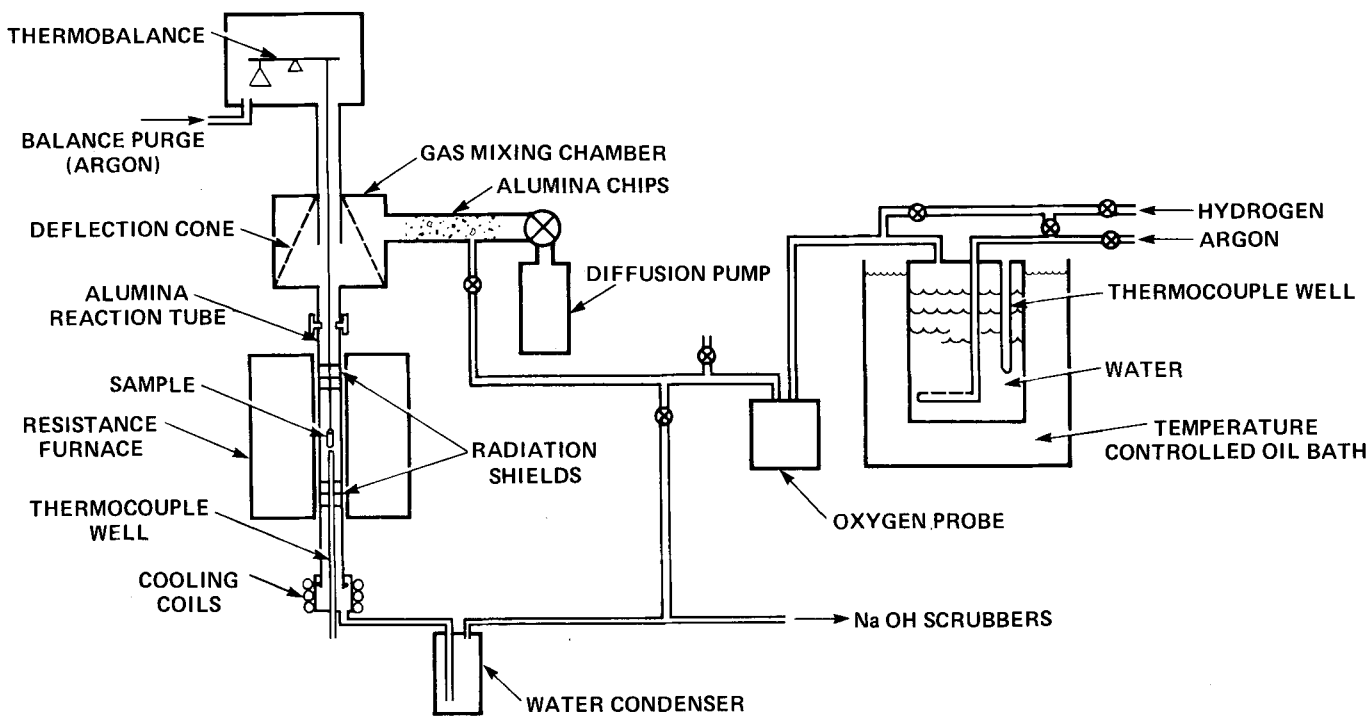

Fig. 1 — Schematic diagram of the corrosion apparatus.

analysis. To permit quantitative analysis, FeS_2 was used as a sulfur standard, and the SAE 310 stainless steel was used as a standard for Fe, Ni, and Cr. In all cases, atomic absorption and fluorescence effects were eliminated using the computer program supplied by NBS called "FRAME-C".

III. RESULTS

A. *Reaction Kinetics*

Corrosion kinetics of SAE 310 stainless steel in hydrogen, water vapor, and hydrogen sulfide gas mixtures at a constant temperature of 1150 K are shown in Figures 2 and 3. Oxygen potential was kept constant at a value of approximately 6×10^{-13} Nm^{-2}, and sulfur potential was varied from 0.19×10^{-2} Nm^{-2} to 33.0×10^{-2} Nm^{-2}. In Figure 2, the data are plotted according to a linear rate equation:

$$(\Delta W/A) = K_l t \qquad [3]$$

where ΔW is weight gain, A is surface area, t is time, and K_l is the linear rate constant. As can be seen, the reaction rate increases with increasing sulfur potential, with pure oxidation giving the lowest reaction rate. An abrupt change in reaction rate occurs in going from a sulfur potential of 2.7×10^{-2} Nm^{-2} to one of 0.19×10^{-2} Nm^{-2}. Additionally, at a sulfur potential of 2.7×10^{-2} Nm^{-2} and above (high sulfur region) the weight gain data are seen (Figure 2) to obey the linear relationship. Below this sulfur potential (low sulfur range) the data obey a parabolic rate equation,

$$(\Delta W/A)^2 = K_p t \qquad [4]$$

where K_p is the parabolic rate constant, as can be seen in Figure 3. Also indicated in Figure 3 is the influence of preoxidation on the simultaneous oxidation-sulfidation reactions. The sample undergoing oxidation in a pure oxygen

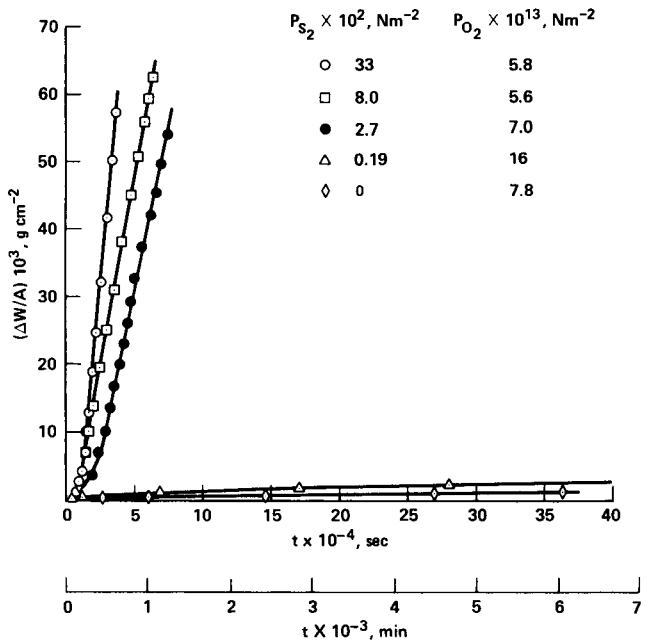

Fig. 2—Kinetic data for SAE 310 stainless steel at 1150 K in H_2-H_2O-H_2S gas mixtures, plotted according to a linear rate law.

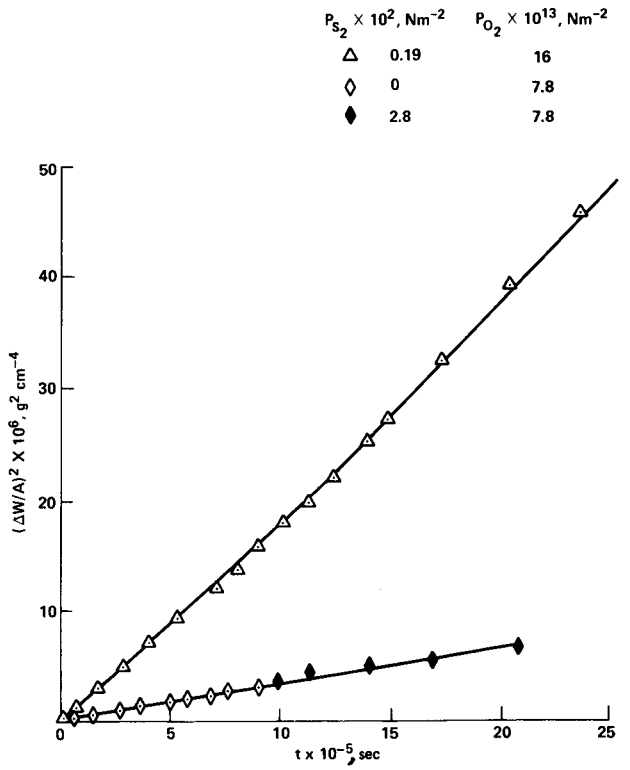

Fig. 3—Kinetic data for SAE 310 stainless steel at 1150 K in H_2-H_2O-H_2S gas mixtures, plotted according to a parabolic rate law.

environment (open diamonds in Figure 3) was exposed to an oxygen-sulfur environment at a sulfur potential of 2.8×10^{-2} Nm^{-2}. As can be seen, the reaction kinetics continued as though only oxygen were present and were unperturbed by the presence of a high sulfur potential (closed diamonds in Figure 3).

In summary, the reaction rate kinetics of 310 stainless steel in a combined oxygen and sulfur environment at the high sulfur region ($P_{S_2} \geq 2.7 \times 10^{-2}$ Nm^{-2}) are fast, approaching those for pure sulfidation, and are linear with time. In the low sulfur region ($P_{S_2} \leq 2.7 \times 10^{-2}$ Nm^{-2}) the reaction rates are slow and the kinetics are parabolic. Finally, preoxidation, at least under the conditions studied here, is capable of inhibiting the sulfidation reaction in a combined oxygen-sulfur environment.

B. *Morphology and Composition of Scales*

Scales at High Sulfur Potentials. The scales formed at high sulfur potentials consist primarily of sulfide phases and are similar to those observed from pure sulfidation.[1,2] The scales are multilayered, containing two outer layers in addition to a subscale. The outermost layer, OL-II (farthest from the alloy), formed at the gas/scale interface consists of sulfide phases that primarily belong to the Fe-Ni-S system. At 1150 K the (Fe,Ni) S phase is a eutectic melt; upon solidification it separated into two phases: a metallic phase, containing approximately 39 pct Fe, 60 pct Ni, and 1 pct S; and a sulfide phase containing approximately 38 pct S, 36 pct Fe, and 26 pct Ni. X-ray analysis of the sulfide indicated that it was a pentlandite phase $(Fe,Ni)_{9-x}S_8$, which may have formed during cooling. Figure 4 shows a typical microstructure and composition of phases of the OL-II layer;

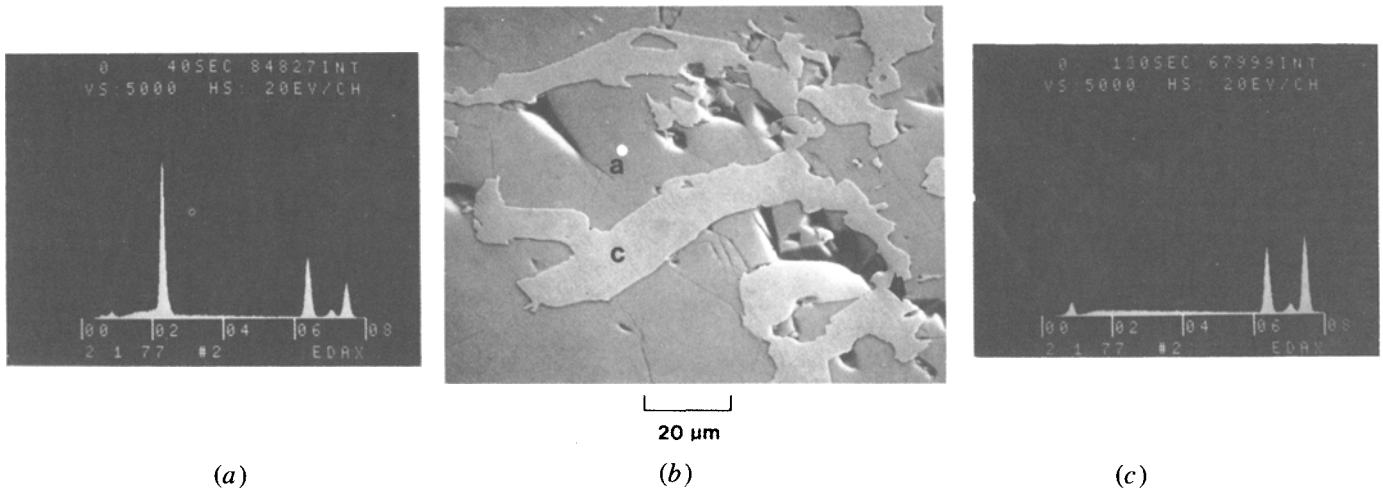

Fig. 4—Microstructure and composition of the corrosion product (OL-II) formed at high sulfur potentials at the gas/scale interface. (*a*) Composition of the sulfide phase (white dot in (b)), (*b*) microstructure of OL-II, (*c*) composition of the metallic phase ("c" on bright phase in (b)). (T = 1150 K, $P_{O_2} = 5.6 \times 10^{-13}$ Nm^{-2}, $P_{S_2} = 8 \times 10^{-2}$ Nm^{-2}, t = 50 h).

Figures 4(a) and 4(c) indicate the compositions of the sulfide phase and the metallic phase, respectively, and Figure 4(b) shows the microstructure of the scale.

The outer layer, OL-I (next to the subscale), consists of phases that belong primarily to the Fe-Cr-S system. In the slowly cooled samples, the microstructure of this layer revealed arrays of alternate sublayers. The sublayers were absent when the reacted samples were quenched—a phenomenon similar to that observed during the pure sulfidation experiments.[2] The energy dispersive X-ray analysis of these layers indicated that they differ only in their Fe : Cr ratio. However, a significant difference between the microstructure of this layer and that due to pure sulfidation is that it contained oxide particles dispersed in the sulfide phase, as shown in Figure 5. This figure shows a typical microstructure and composition of phases of the outer layer (OL-I); Figures 5(a) and 5(c) indicate the compositions of the sulfide phase and the oxide phase, respectively, and Figure 5(b) shows the microstructure of the scale. The diameters of the oxide particles are seen to be of the order of 2 to 20 μm, and the particles consist primarily of (Fe,Mn) Cr_2O_4. These particles were found mainly at the scale/subscale interface where the reaction between the alloy and the gas phase initiated. The composition of the sulfide phase is not fixed. The chromium content of the sulfide increased gradually from the OL-II/OL-I interface to OL-I/subscale interface. Again, this is a striking similarity to pure sulfidation.[2] The iron content of the oxide phase was approximately 5 wt pct.

The subscale consisted of sulfide inclusions in the alloy, and the sulfide phases were chromium and manganese rich. The nature of the subscale is once again similar to that of pure sulfidation.[1,2]

Scales at Low Sulfur Potentials. At the low sulfur potential ($P_{S_2} = 0.19 \times 10^{-2}$ Nm^{-2}) the scale was predominantly an oxide. The microstructure and the K_α X-ray mappings for various elements are shown in Figure 6. It is seen that a continuous sulfide does not exist. However, iron sulfide did form as a discontinuous layer at the gas/scale interface after a reaction time of about 1200 hours. The primary scale is a chromium-rich oxide scale, and a variation in the composition of the scale from a spinel, (Fe,Mn) Cr_2O_4, to mainly chromium oxide can be noticed. Beneath the chromium oxide layer a thin layer of silicon dioxide was observed. The silicon dioxide extended to the grain boundaries of the subscale region, as can be seen from the silicon mapping in Figure 6. Discrete particles of chromium- and manganese-rich sulfides are also formed in the subscale. X-ray mapping reveals an absence of iron and nickel in the internally formed sulfide precipitates.

The concentration profiles of various elements in the scale, as analyzed by the energy dispersive X-ray analysis, are shown in Figure 7. In calculating the concentration profiles, it was assumed that the sum of concentrations of Cr, Mn, Fe, Ni, Si, and S equals 100, and oxygen was ignored. X-ray diffraction patterns showed the presence of (Fe, Mn) Cr_2O_4 and Cr_2O_3.

C. *Preoxidation*

The structure and composition of the scale formed upon preoxidation followed by simultaneous oxidation-sulfidation at high sulfur potential was almost identical to that of the simultaneous oxidation-sulfidation at low sulfur potential. The only difference was the absence of internal precipitates of sulfides, as shown in Figure 8, whereas in the case of simultaneous oxidation-sulfidation at low sulfur potential without preoxidation, the scales did show the formation of internal sulfides (Figure 7). The composition profiles of the various elements in the scale that formed upon preoxidation followed by simultaneous oxidation sulfidation is shown in Figure 8.

D. *Thermochemical Diagrams*

The value of thermochemical diagrams in predicting and correlating the compositions of corrosion scales as a function of alloy composition, in visualizing a reaction path, and in explaining the formation of nonequilibrium phases due to variation in experimental conditions has been demonstrated with respect to sulfidation of 310 stainless steel in a previous publication.[3] A comparison of experimental data and those

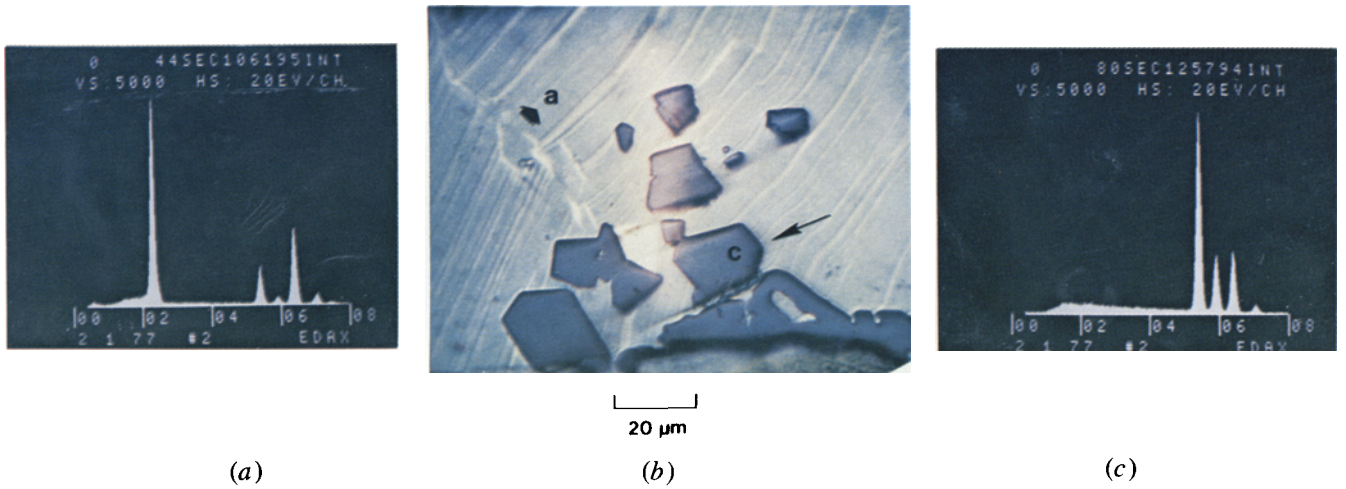

Fig. 5—Microstructure and composition of the corrosion product (OL-I) formed at low sulfur potentials at the scale/subscale interface. (*a*) Composition of the sulfide phase ("a" in (b)), (*b*) microstructure of OL-I, (*c*) composition of the oxide islands ((Fe,Mn) Cr_2O_4) ("c" in (b)). (T = 1150 K, $P_{O_2} = 5.6 \times 10^{-13}$ Nm^{-2}, $P_{S_2} = 8 \times 10^{-2}$ Nm^{-2}, t = 50 h).

deduced from the thermochemical diagrams helps provide guidelines for the future development of corrosion resistant alloys.

Thermochemical diagrams can be constructed in many ways, depending on which of the parameters (temperature, composition, partial pressure of a nonmetallic component, chemical potential, *etc.*) are used to define the axes of a diagram. A plot of the logarithm of the partial pressure of the nonmetallic components at a constant temperature seems best because the information on corrosion characteristics of an alloy can be gathered more appropriately from such diagrams. The effects of changes in alloy composition on the morphology and composition of corrosion scales can be readily visualized on these types of plots. Phase diagrams of this type have been constructed for three component systems; they were reported in a previous publication.[3] In four component systems, where more than one nonmetallic reactive element is involved, the representation of the phase

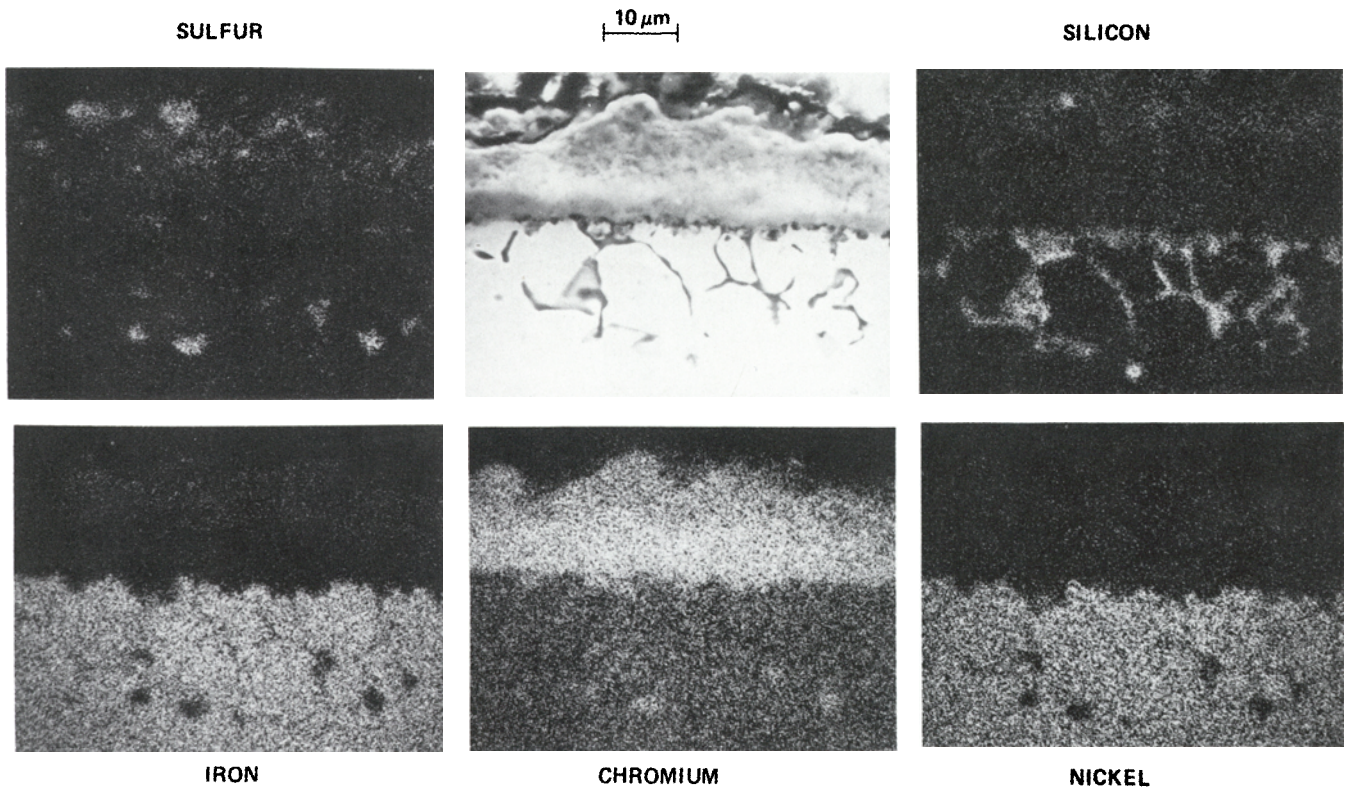

Fig. 6—Microstructure and K_α X-ray mapping for the various elements of the corrosion product formed at low sulfur potentials (T = 1150 K, $P_{O_2} = 1.6 \times 10^{-12}$ Nm^{-2}, $P_{S_2} = 1.9 \times 10^{-3}$ Nm^{-2}, t = 1200 h).

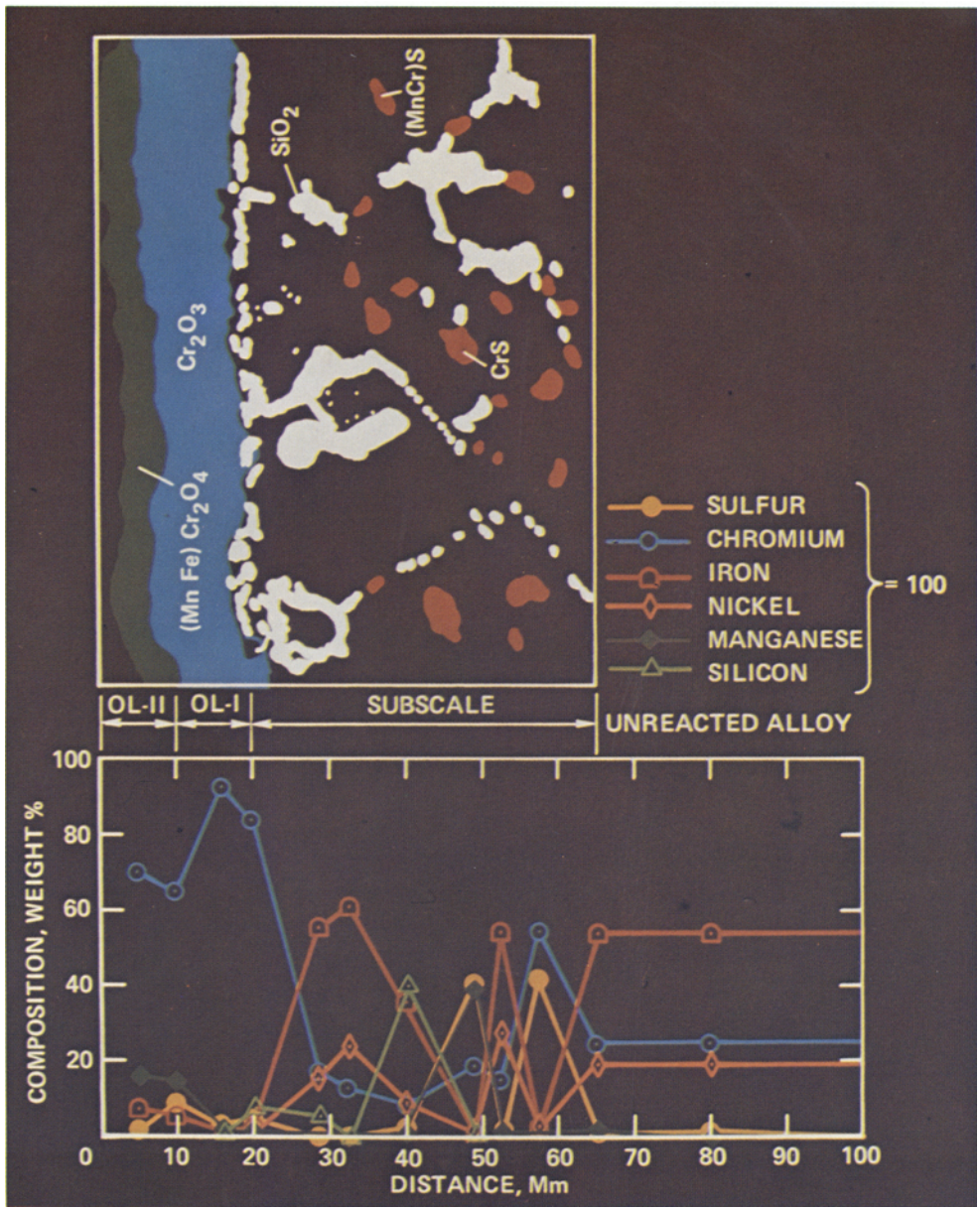

Fig. 7—Concentration profiles for the various elements in the scale formed at low sulfur potentials, as determined by energy dispersive X-ray analysis (T = 1150 K, P_{O_2} = 1.9 × 10^{-12} Nm^{-2}, P_{S_2} = 1.4 × 10^{-3} Nm^{-2}, t = 1200 h).

diagrams must be three dimensional unless the temperature and partial pressure of one of the nonmetallic elements are constant. Because the experimental data reported in this paper were obtained at a fixed temperature of 1150 K and a fixed oxygen potential of 6 × 10^{-13} Nm^{-2}, the stability field diagrams were developed under the same conditions to facilitate direct comparison. It should, however, be kept in mind that these diagrams are sections of the three-dimensional plots.

The stability field diagrams constructed at a constant temperature of 1150 K and at constant oxygen potential of 6 × 10^{-13} Nm^{-2} for Fe-Cr-S-O, Fe-Ni-S-O, Cr-Ni-S-O, and Si-Cr-S-O are shown in Figures 9 through 12. A detailed description of the methods adopted to estimate the unknown thermal data for some of the ternary sulfides, spinels, and solid solutions is described elsewhere.[3]

Fe-Cr-S-O. Stability fields for the compounds in the system Fe-Cr-S-O at a temperature of 1150 K and a fixed oxygen potential of 6 × 10^{-13} Nm^{-2} are depicted in Figure 9. It is clear from this figure that below the sulfur potential of 10^{-3} Nm^{-2} for a mole fraction of chromium corresponding to 310 stainless steel composition (indicated by the arrow on the abscissa of Figure 9), the stable phases that are expected to form are α Fe and $FeCr_2O_4$. In the range of sulfur potentials between 10^{-3} Nm^{-2} and 10 Nm^{-2}, the Fe(Cr)S phase rich in Fe with less than 1.25 pct of Cr is expected to form along with $FeCr_2O_4$. In the sulfur potential range from 10 Nm^{-2} to 10^{3} Nm^{-2} the solid solution Fe-Cr-S with higher

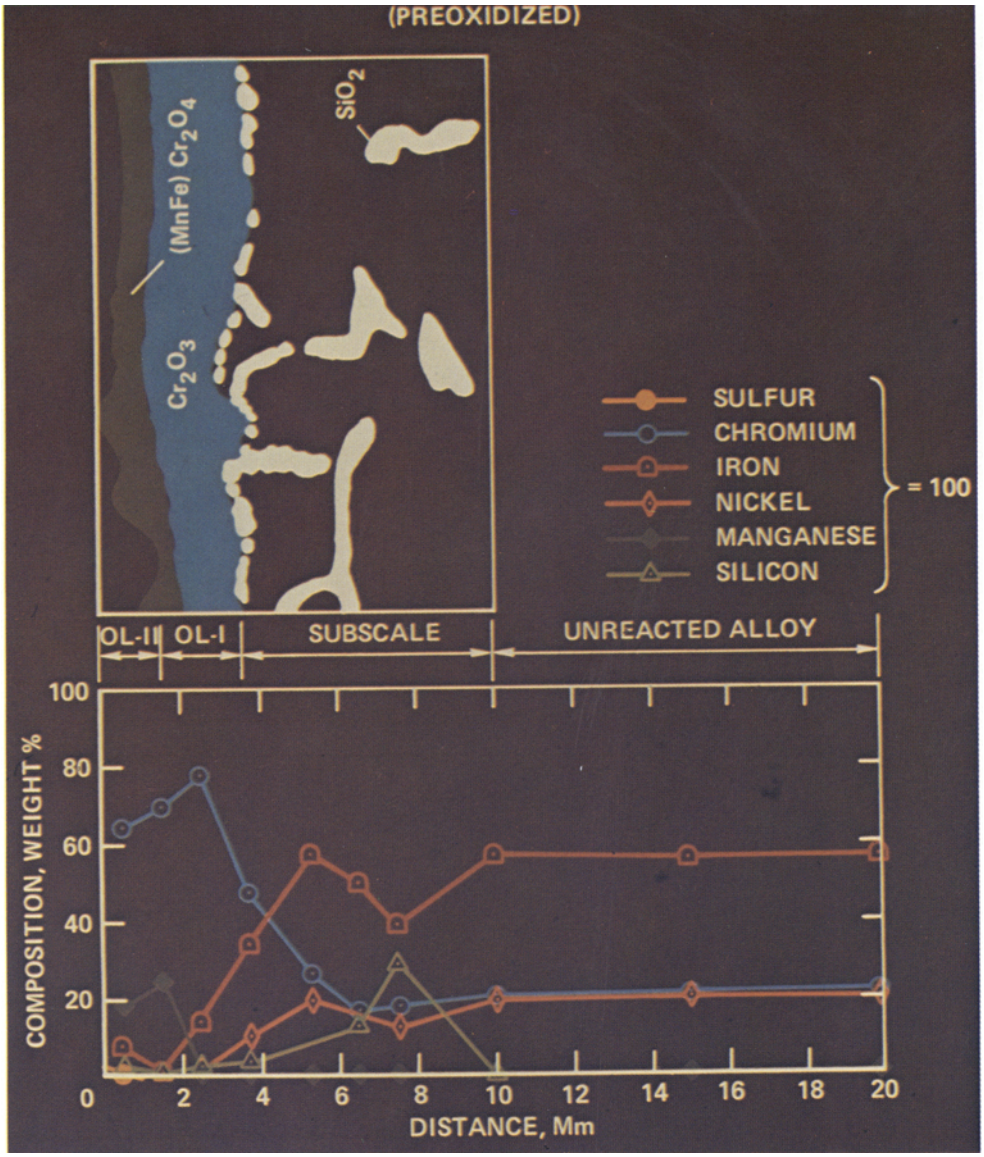

Fig. 8—Concentration profiles for the various elements in the scale formed at high sulfur potentials, after preoxidation as determined by energy dispersive X-ray analysis (T = 1150 K, $P_{O_2} = 7 \times 10^{-13}$ Nm^{-2}, $P_{S_2} = 2.8 \times 10^{-2}$ Nm^{-2}, t = 600 h).

Cr concentrations is expected to form along with Cr_2O_3. The $FeCr_2O_4$ phase will be unstable. At sulfur potentials above 10^3 Nm^{-2} both iron and chromium form sulfides and the oxides (Cr_2O_3 and $FeCrO_4$) are unstable. Preliminary calculations on phase relations in the Fe-Mn-Cr-S-O system indicate that even small amounts of Mn in the alloy would result in a spinel phase (Fe,Mn) Cr_2O_4 in which significant Mn substitution for Fe takes place.

Fe-Ni-S-O. Stability fields for the compounds in the system Fe-Ni-S-O at a temperature of 1150 K and at a fixed oxygen potential of 6×10^{-13} Nm^{-2} are shown in Figure 10. It is evident that at sulfur potentials above 10^{-3} Nm^{-2}, sulfides of Fe and Ni form and the oxides are unstable. At sulfur potentials below 10^{-3} Nm^{-2} iron and nickel will neither oxidize nor sulfidize. However, it is clear from Figure 9 that in the presence of chromium, iron oxidizes below the sulfur potential of 10^{-3} Nm^{-2} to form $FeCr_2O_4$.

Ni-Cr-S-O. The stability field diagram for Ni-Cr-S-O shown in Figure 11 is similar to that of Fe-Cr-S-O, except that the $NiCr_2O_4$ is unstable at an oxygen potential of 6×10^{-13} Nm^{-2}. Moreover, in the corrosion of 310 stainless steel the formation of ternary and quaternary compounds belonging to the Cr-Ni-S, Cr-Ni-O, or Cr-Ni-S-O systems were never experimentally observed.

Si-Cr-S-O. The Si-Cr-S-O stability field diagram, which is relatively simple, is shown in Figure 12. The Cr_2O_3 is stable up to a sulfur potential of about 3.2×10^3 Nm^{-2}. Above this sulfur potential Cr_2S_3 is expected to form.

E. *Comparison of Experimental Results and Thermochemical Diagrams*

It can be inferred from the thermochemical diagrams that $FeCr_2O_4$ is the main corrosion product to expect at a sulfur

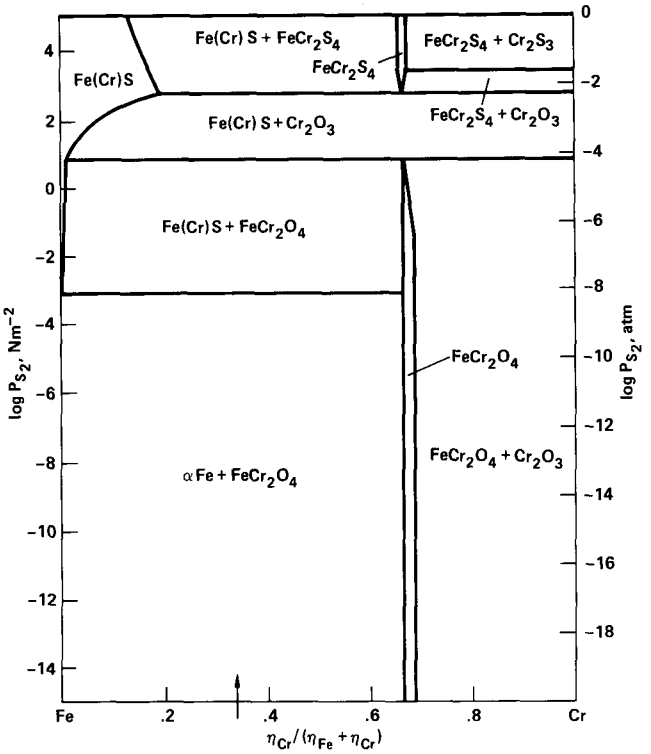

Fig. 9 — Thermochemical diagram for the Fe-Cr-S-O-system (T = 1150 K, $P_{O_2} = 6 \times 10^{-13}$ Nm^{-2}).

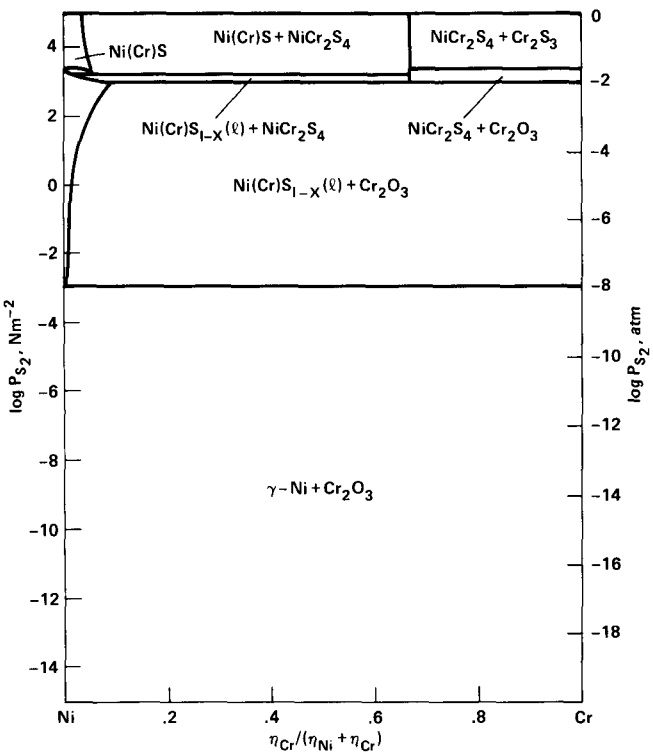

Fig. 11 — Thermochemical diagram for the Ni-Cr-S-O system (T = 1150 K, $P_{O_2} = 6 \times 10^{-13}$ Nm^{-2}).

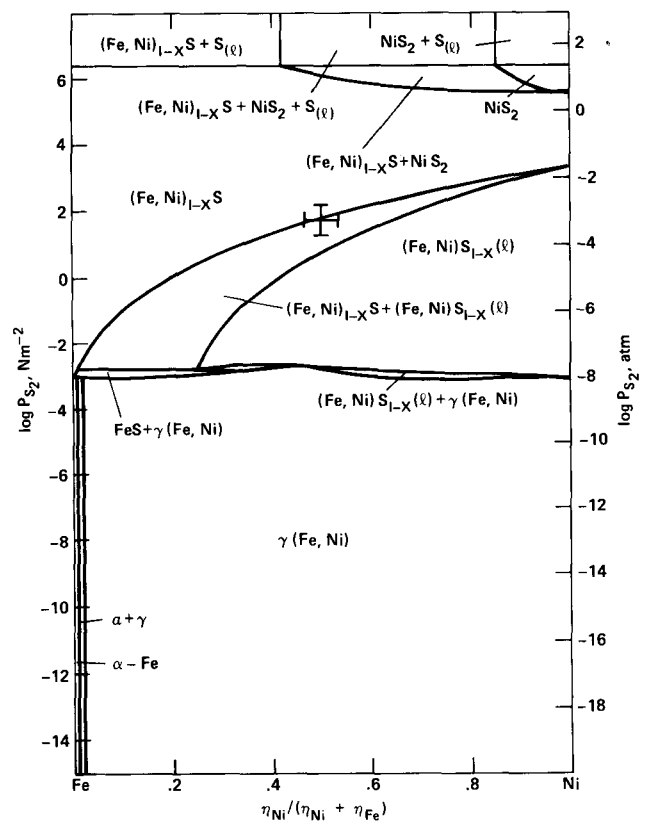

Fig. 10 — Thermochemical diagram for the Fe-Ni-S-O system (T = 1150 K, $P_{O_2} = 6 \times 10^{-13}$ Nm^{-2}).

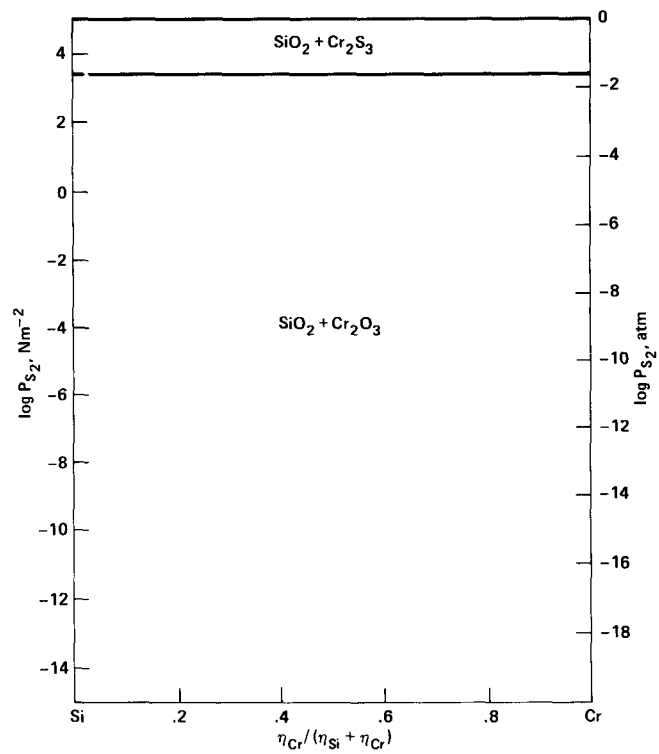

Fig. 12 — Thermochemical diagram for the Si-Cr-S-O system (T = 1150 K, $P_{O_2} = 6 \times 10^{-13}$ Nm^{-2}).

potential of 1.9×10^{-3} Nm^{-2} (low-sulfur potential region). Thermochemical calculations also indicate that the presence of Mn in SAE 310 would result in the formation of a mixed spinel (Fe,Mn) Cr_2O_4. Sulfide phases are not expected to form in the Fe-Ni-S system, and chromium preferentially forms an oxide. Experimentally, the outermost layer (OL-II) was composed of (Fe,Mn) Cr_2O_4 (Figure 7), as would be expected. The formation of Cr_2O_3 as the primary phase in OL-I (Figure 7) will be discussed in greater detail in the next section. The formation of chromium oxide results in the depletion of iron and chromium and the enrichment of the minority element, Si, allowing SiO_2 to form beneath Cr_2O_3, as was observed (Figure 7).

At high sulfur potentials ($P_{S_2} \geq 2.7 \times 10^{-2}$ Nm^{-2}), the products that are expected to form are $FeCr_2O_4$; Fe(Cr)S, with chromium content less than 1 pct in the Fe-Cr-S-O system; and (Fe,Ni) S(l). Experimentally, it was observed that (Fe,Mn) Cr_2O_4 formed only as islands dispersed in the (Fe,Cr) S phase (Figure 5). The composition of the (Fe,Cr) S phase varied with chromium concentration, increasing up to 30 wt pct moving from the interface OL-II/OL-I to the interface OL-I/subscale (Figure 8). Thus, the products that are expected to form on the basis of thermochemical calculation were observed. However, as will be explained in the next section, the composition of the (Fe,Cr)S phase contained much more chromium than predicted from the quaternary diagrams, and a continuous protective layer of (Mn,Fe) Cr_2O_4 did not form. The observed composition of the (Fe,Cr) S is in better agreement with preliminary calculations on the pentanary system Fe-Ni-Cr-S-O. The pentanary calculations are highly complex, and the equilibria cannot be readily sketched in two dimensions.

IV. DISCUSSION

The experimental results indicate that the corrosion of 310 stainless steel at a constant temperature of 1150 K and at a constant oxygen potential of 6×10^{-13} Nm^{-2} can be either sulfidizing or oxidizing, depending on the sulfur potential at which the samples are reacted. At a sulfur potential of 1.9×10^{-3} Nm^{-2}, the corrosion products are exclusively oxides — (Fe,Mn) Cr_2O_4, Cr_2O_3, and SiO_2 (Figure 7) — and the reaction rates obey a parabolic rate law (Figure 3). After prolonged reaction times ($t \approx 1000$ hours), small amounts of FeS started to form at the gas/scale interface. At higher sulfur potentials ($P_{S_2} \geq 2.7 \times 10^{-2}$ Nm^{-2}) the corrosion scale layers are sulfides and their compositions were almost identical to those formed during pure sulfidation.[2] The exception was the presence of oxide particles in the OL-I layer near the subscale interface (Figure 5). Additionally, the reaction rates were linear and thus different from the parabolic kinetics observed in the case of pure sulfidation.[1]

A. *Corrosion Mechanism at Low Sulfur Potentials*

At low sulfur potentials where iron and nickel sulfides are unstable, the only corrosion products that form are the oxides — (Fe,Mn) Cr_2O_4, Cr_2O_3, and SiO_2. These products were observed as separate layers, as shown in Figure 7. Because the order of formation of these layers is unknown, it is difficult to determine the exact mechanism of corrosion. However, some insight can be gained from previous work performed on other systems. Bernard *et al*[5] investigated the oxidation mechanism of austenitic stainless steel (18 pct Cr-8 pct Ni) at 1323 K in air. They were able to distinguish three oxidation periods. The first period was characterized by a slow oxidation, where X-ray and electron diffraction analyses indicate that the oxide layer is composed of $FeCr_2O_4$ and Cr_2O_3. This period was found to last for more than 100 hours, depending on the chromium content of the alloy. The oxidation rate obeyed a parabolic rate law. The second period was characterized by rapid oxidation where the formation of α Fe_2O_3 was observed. The third period was characterized by slow oxidation.

In the present study oxidation was confined to a much lower oxygen potential, and the steel, which was of commercial quality, had a composition that was significantly different from that studied by Bernard *et al.*[5] A slight increase in the corrosion rate after a reaction period of about 500 hours may have occurred in the present experiments (Figure 3), but the change was not great enough to be interpreted as a separate regime. Additionally, it is possible that a change in corrosion rate may not have occurred at these low oxygen potentials, where Fe_2O_3 will not form. Moreover, because of the complex chemical nature of commercial 310 stainless steel, the formation of (Fe,Mn) Cr_2O_4 was observed in contrast to the $FeCr_2O_4$ observed by Bernard *et al.*

It is, therefore, tentatively proposed that initially (Fe,Mn) Cr_2O_4 forms as a continuous layer. Corrosion proceeds by cation diffusion through this layer to the gas/scale interface. With the growth of the spinel layer, the oxygen potential at the scale/subscale interface would be less than in the gas phase. Consequently, chromium activity at the scale/subscale interface would increase. At oxygen potentials lower than that existing in the gas phase, the spinel phase becomes unstable and decomposes into Cr_2O_3. For example, $FeCr_2O_4$ would decompose into Cr_2O_3 at an oxygen potential of 8.68×10^{-17} Nm^{-2} (Reference 6). This decomposition can be represented as an exchange reaction,

$$3(Fe,Mn)Cr_2O_4 + 2Cr \rightarrow 4Cr_2O_3 + 3Fe + 3Mn \quad [5]$$

which takes place at the interface of outer layers II and I. The Fe, Mn, and Cr diffusing out would oxidize at the gas/scale interface to form (Fe,Mn) Cr_2O_4. In this case the thickness of (Fe,Mn) Cr_2O_4 layers formed would remain either relatively independent of time after attaining a critical thickness or grow at a relatively slower rate than the formation of the Cr_2O_3 layer. Since part of the chromium flux from the alloy to the scale/gas interface is consumed by the exchange reaction [5], it is likely that the flux of iron diffusing to the gas/scale interface will be higher than that required to form the spinel. Since FeO is unstable at the oxygen pressure prevailing in the gas, the excess iron would form sulfides. A discontinuous iron sulfide layer was in fact observed after prolonged exposure (1200 hours). The oxidation of chromium results in the depletion of chromium and the enrichment of Si in the alloy facilitating the formation of SiO_2 at the scale/alloy interface.

B. *Corrosion Mechanism at High Sulfur Potentials*

The high corrosion rate at high sulfur potentials, where no protective oxide layer was observed, is significantly greater than the corrosion rate observed at low sulfur potentials.

Thermochemical diagrams predict the formation of oxides, but only (Fe,Mn) Cr_2O_4 was formed as islands embedded in a (Fe,Cr) S phase (Figure 5). The (Fe,Cr) S phase is unstable in the presence of oxygen, according to thermochemical diagrams, because chromium should preferentially react with oxygen to form oxide. In a sulfur environment at high sulfur potentials, Fe and Ni will form sulfides.

Three stages of the reaction were observed, as shown schematically in Figure 13. At the onset of the corrosion reaction (Stage I) both (Fe,Mn) Cr_2O_4 and (Fe,Ni) S form as separate nuclei. Because of the higher diffusion rate through the sulfides, the sulfide islands grow at a relatively faster rate than the oxide islands (Stage II). Once Stage II is reached, the gas phase is separated from the alloy and chromium is isolated from the oxygen. Consequently, the oxide islands cease to grow and a protective oxide layer cannot form. After the formation of a continuous (Fe,Ni) S layer an exchange reaction,

$$(Fe,Ni)S + Cr \rightarrow (Fe,Cr)S + Ni \qquad [6]$$

will take place at the interface (shown as B in Figure 13; Stage III). The species Fe and Ni will diffuse out to the gas/scale interface (A in Figure 13) and will react with sulfur to again form the (Fe,Ni) S phase. Thus, the (Fe,Cr) S phase is stabilized below the (Fe,Ni)S layer, resulting in the morphology of corrosion layers similar to that of pure sulfidation, except for the formation of the oxide islands in the (Fe,Cr) S phase. Because the primary corrosion reaction is controlled at the interface B (Figure 13), which remains stationary, the corrosion rate is linear with time. A difference in the kinetic rates among these three stages was not observed, probably because of the very high reaction rates. It should be emphasized that, in the pure sulfidation experiments,[1] the (Fe,Cr) S phase formed initially and the (Fe,Ni)S phase formed later.

C. *Effect of Preoxidation*

During preoxidation, continuous protective layers of (Fe,Mn) Cr_2O_4 and Cr_2O_3 were formed, similar to those observed at low sulfur potentials. These layers restrict the outward diffusion of nickel and the inward diffusion of sulfur, even at high sulfur potentials. Thus, a careful preoxidation at low oxygen potentials is extremely beneficial.

V. CONCLUSIONS

Simultaneous oxidation-sulfidation of SAE 310 at a constant temperature of 1150 K and a constant oxygen potential of about 6×10^{-13} Nm^{-2} can be categorized into two regions: a high sulfur potential region ($P_{S_2} > 10^{-2}$ Nm^{-2}) and a low sulfur potential region ($P_{S_2} \leq 10^{-3}$ Nm^{-2}). At high sulfur potentials, the corrosion scales are mainly sulfides, (Fe,Ni) S and (Fe,Cr) S. At high sulfur potentials, the corrosion rates are high and the kinetics obey a linear rate equation. At low sulfur potentials, the corrosion scales are mainly oxides, (Fe,Mn) Cr_2O_4 and Cr_2O_3. At low sulfur potentials, the corrosion rates are slow and the kinetics obey a parabolic rate equation. Preoxidation at 1150 K and at an oxygen potential of 6×10^{-13} Nm^{-2} helps to develop protective oxide scale and reduces the corrosion rate substantially at high sulfur potentials. Thermochemical calculations indicate that the stable phases at high sulfur potentials are (Fe,Mn) Cr_2O_4, $FeCr_2O_4$, and (Fe,Ni) S. At low sulfur potentials, the stable phases are (Fe,Mn) Cr_2O_4 and $FeCr_2O_4$. Tentative mechanisms based on the experimental observations are proposed. The mechanism of corrosion at high sulfur potentials comprises (1) the initial nucleation of the (Fe,Mn) Cr_2O_4 and (Fe,Ni) S phases, simultaneously, (2) overgrowth of the (Fe,Ni) S phase to form a continuous layer, and (3) the displacement reaction of (Fe,Ni) S with chromium to form (Fe,Cr) S at the scale/subscale interface to form duplex scales. At low sulfur potentials, (Fe,Mn) Cr_2O_4 forms initially as a continuous layer, and corrosion proceeds by cation diffusion through this layer. With the growth of this spinel layer, the oxygen potential at scale/subscale interface would be less than in the gas phase. Consequently, chromium activity at this interface would increase, facilitating an exchange reaction with chromium to form Cr_2O_3.

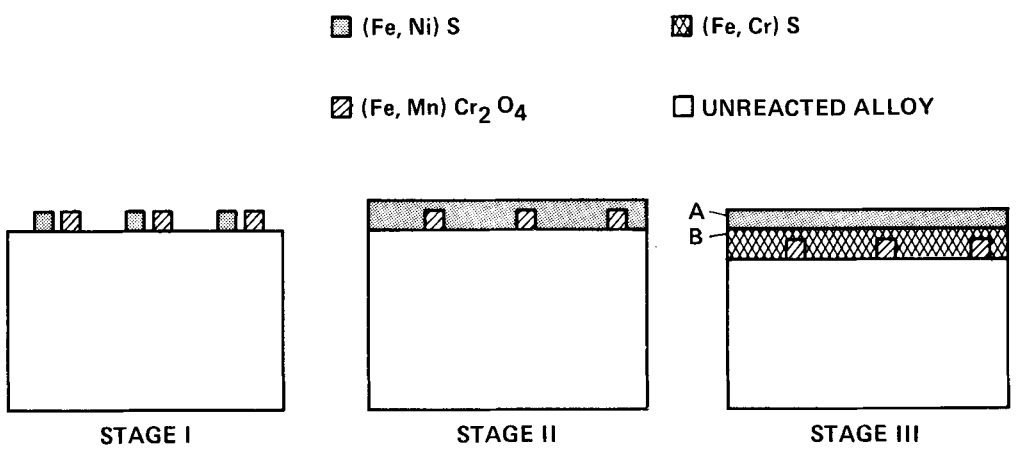

Fig. 13 — Schematic of the corrosion mechanism suggested to be operative at low oxygen and high sulfur potentials.

REFERENCES

1. D. B. Rao and H. G. Nelson: (NASA Technical Memorandum 73,116, 1976), *Proc. Symposium on Properties of High Temperature Alloys*, Electrochemical Soc., Princeton, NJ, 1977, vol. 77-1, 2A, pp. 464-92.
2. D. B. Rao and H. G. Nelson: (NASA Technical Memorandum 73,246, 1977), *Oxidation of Metals*, 1978, vol. 12, pp. 111-38.
3. K. T. Jacob, D. B. Rao, and H. G. Nelson: (NASA Technical Memorandum 78,465, 1977), *Oxidation of Metals*, 1979, vol. 13, pp. 25-55.
4. JANAF Thermochemical Tables, NSRDS-NBS 37, 1974.
5. J. Bernard, J. Hertz, Y. Jeannin, and J. Moreau: *C. R. Acad. Sci. Ser. A*, 1959, vol. 248, p. 2095.
6. K. T. Jacob and C. B. Alcock: *Metall. Trans. B*, 1975, vol. 6B, pp. 215-21.